White Rose Research Online
eprints@whiterose.ac.uk
https://eprints.whiterose.ac.uk
Universities of Leeds, Sheffield and York

Deposited via The University of Leeds.

White Rose Research Online URL for this paper:
https://eprints.whiterose.ac.uk/id/eprint/238320/

Version: Accepted Version

Article:
Sun, J., Huang, W., Qin, Y. et al. (2026) Multi-Physical Properties of Epoxy Asphalt Under Component Variations: A Molecular Dynamics Simulation and Experimental Study. Journal of Applied Polymer Science. e70532. ISSN: 0021-8995

https://doi.org/10.1002/app.70532

This is an author produced version of an article published in the Journal of Applied Polymer Science, made available via the University of Leeds Research Outputs Policy under the terms of the Creative Commons Attribution License (CC-BY), which permits unrestricted use, distribution and reproduction in any medium, provided the original work is properly cited.

Reuse
This article is distributed under the terms of the Creative Commons Attribution (CC BY) licence. This licence allows you to distribute, remix, tweak, and build upon the work, even commercially, as long as you credit the authors for the original work. More information and the full terms of the licence here: https://creativecommons.org/licenses/

Takedown
If you consider content in White Rose Research Online to be in breach of UK law, please notify us by emailing eprints@whiterose.ac.uk including the URL of the record and the reason for the withdrawal request.

UNIVERSITY OF LEEDS
University of Sheffield
UNIVERSITY of York

Multi-Physical Properties of Epoxy Asphalt Under Component Variations: A Molecular Dynamics Simulation and Experimental Study

Jia Sun [a], Wei Huang [b], Yu Qin [a, e], Zhihan Zhang [a], Zixuan Ling [a], Ali Rahman [c], Yue Huang [d], Sang Luo [b, *]

[a] *School of Transportation, Southeast University, Nanjing, Jiangsu, 211189, P. R. China*

[b] *Intelligent Transportation System Research Center, Southeast University, Nanjing, Jiangsu, 211189, P. R. China*

[c] *School of Civil Engineering, University of Leeds, Leeds, LS2 9LG, UK*

[d] *Institute for Transport Studies, University of Leeds, Leeds, LS2 9JT, UK*

[e] *Nanjing Modern Multimodal Transportation Laboratory, Nanjing, Jiangsu, 211100, P. R. China*

***Corresponding author:**

Name: Sang Luo

Address: Intelligent Transportation System Research Center, Southeast University, Nanjing, Jiangsu, 211189, P. R. China

E-mail: 101011363@seu.edu.cn

Table of Contents

This study establishes molecular dynamics (MD) models of epoxy asphalt (EA) with varying compositions. In conjunction with experiments, it investigates the evolution of the multi-physical properties of EA with increasing epoxy content, validating the consistent trends between simulations and experiments. This approach overcomes the limitations of traditional testing, providing molecular-level insights into the performance evolution of EA and facilitating its optimal design and application.

Graphical Abstract

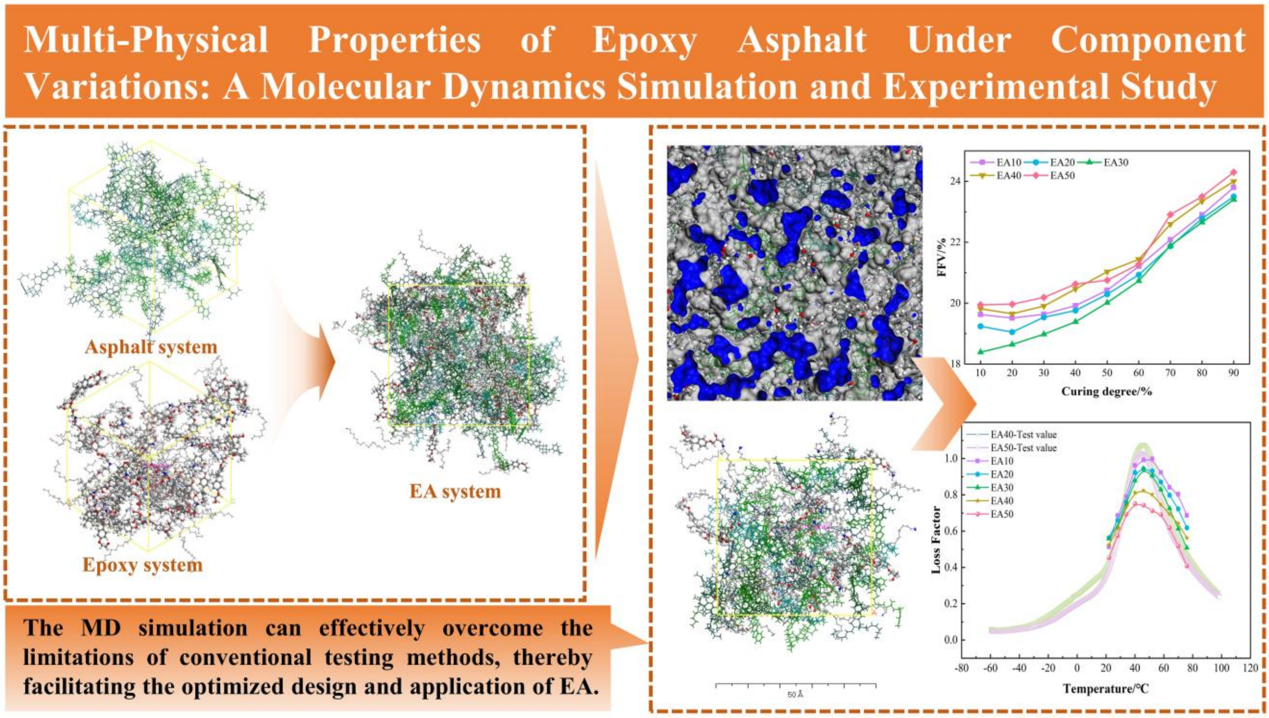

Multi-Physical Properties of Epoxy Asphalt Under Component Variations: A Molecular Dynamics Simulation and Experimental Study

The MD simulation can effectively overcome the limitations of conventional testing methods, thereby facilitating the optimized design and application of EA.

Abstract: A lack of unified testing and evaluation methods for both thermoplastic and thermosetting epoxy asphalt (EA) impedes the characterization of its performance evolution across varying epoxy resin system (EPS) contents, thereby limiting its optimal design. To address this gap, this study constructed and validated molecular models reflecting different EPS contents and curing degrees. Key thermal, volumetric, and mechanical properties were calculated via simulation and comprehensively analyzed alongside experimental results to understand the evolution of the physical characteristics of EA. The findings indicate that the volumetric features and glass transition behavior of EA are significantly influenced by both EPS content and curing degree. A critical transition from an asphalt-dominated thermoplastic state to a crosslinked-network-controlled thermosetting state begins at 30 wt% EPS. While increasing EPS content enhances heat resistance, its higher thermal expansion adversely affects the volumetric stability of the material. Notably, EA40 (40 wt% EPS) demonstrates a superior balance between stiffness and damping performance over EA50. Moreover, MD simulations successfully overcame experimental limitations, revealing consistent trends in modulus evolution and the ductile-to-brittle transition with increasing EPS content. These results offer molecular-level insights into the performance evolution of EA, promoting its design for diverse and multi-scenario applications.

Keywords: Epoxy asphalt; Molecular dynamics simulation; Performance evolution; Volumetric parameters; Rheological properties; Pavement materials

1. Introduction

With the acceleration of urbanization and continuous growth in transportation demand, road traffic environments have become increasingly complex, experiencing rising traffic volumes and heavier loads (R. Li et al. 2019; Nieuwenhuijsen 2016). Under extreme climate conditions, heavy traffic loads, and complex stress environments, conventional asphalt pavement materials commonly face challenges such as high-temperature rutting deformation, low-temperature cracking, and insufficient fatigue life. Their service performance and durability often fail to meet the requirements for long service life and high reliability in modern transportation systems (Almeida and Picado-Santos 2022; Qiao et al. 2020). In this context, researchers have focused on developing high-performance polymer-modified asphalt materials, including carbon nanotube (CNT) modified asphalt, polyurethane (PU) modified asphalt, and epoxy asphalt (EA) (ul Haq et al. 2020; Jiang et al. 2023; H. Liu, Zhang, et al. 2022). Among these, as a high-performance pavement material obtained through chemical modification, EA has attracted widespread attention due to its excellent mechanical properties and durability.

EA is a polymer-modified bituminous material composed of epoxy resin, curing agent, and base binder. Benefiting from the cross-linked network structure formed during curing reactions, EA exhibits superior performance to conventional asphalt in terms of high-temperature stability, moisture resistance, and fatigue life (Sun et al. 2022; Z. Zhang et al. 2021). Currently, EA has been successfully applied in deck pavements of numerous long-span steel bridges worldwide, including the Golden Gate Bridge (USA), Akashi Kaikyo Bridge (Japan), and Hangzhou Bay Bridge (China) (Y. Liu, Shen, et al. 2022; Bocci and Canestrari 2012). Field applications demonstrate that steel bridge decks paved with high-performance EA show significantly enhanced structural stability and durability, while effectively reducing maintenance frequency and lifecycle costs. However, the high production cost currently restricts EA applications to specialized scenarios such as steel bridge deck pavements and airport runways (Sun, Luo, Huang, and Li 2023; Sun, Luo, Huang, Hu, et al. 2023). Given its technical advantages, EA also holds promising potential for high-stress, long-service-life applications like heavy-duty highway sections and urban arterial roads. Therefore, exploring diversified applications of EA is of significant importance for promoting its technological advancement and broader implementation.

It is noteworthy that the performance of EA is significantly influenced by its component ratios, particularly the content of the epoxy resin system (EPS). As the EPS content increases from low to high concentrations, EA undergoes a distinct transition in its material behavior, shifting from a thermoplastic state with asphalt as the continuous phase to a thermosetting state dominated by the cross-linked network structure (Sun, Huang, et al. 2023). This transformation leads to a marked performance shift, that is, low-EPS systems may retain some creep recovery capability but with limited strength, whereas high-EPS systems demonstrate significantly enhanced stiffness and strength but may exhibit increased brittleness (F. Zhang et al. 2023; Chen et al. 2024). However, this fundamental change in thermal behavior makes it challenging to establish a unified physical performance testing standard. This limitation not only hinders systematic research on the performance evolution of EA but also obstructs efficient material development and design.

Under these circumstances, molecular dynamics (MD) simulation has emerged as an advanced technical approach capable of revealing structure-property relationships at the microscopic level, gradually gaining attention in asphalt materials research. This methodology elucidates the interaction mechanisms between polymers and asphalt components by constructing molecular structure models, thereby explaining the fundamental reasons behind macroscopic performance variations (Yao et al. 2022; Nie, Chow, and Lau 2022). Currently, several researchers have applied MD simulations to EA investigations. Cheng et al. employed a combined approach of molecular dynamics simulation and experimental methods to study the compatibility mechanism between epoxy resin and asphalt, as well as its influence on EA performance. Their results demonstrated optimal compatibility between asphaltene/resin components and epoxy resin at 160°C preparation temperature with 40 wt% epoxy resin content, where the strongest intermolecular interactions and optimal dispersion were achieved

(Cheng et al. 2025). Li et al. investigated the performance evolution of EA with different crosslinking network densities during photo-oxidative aging by adjusting composite curing agent ratios. Their findings revealed that increasing anhydride curing agent proportion effectively inhibited oxygen diffusion and carbonyl formation. Additionally, high crosslinking density systems mitigated aging-induced negative effects on glass transition temperature and phase compatibility, though asphaltene aggregation was promoted (M. Li, Min, Ouyang, et al. 2023). Shan et al. modified EA with epoxidized soybean oil (ESO) to examine its effects on mechanical properties and compatibility. The results showed that at 10% ESO content, the modified EA exhibited optimal comprehensive performance. MD simulations revealed that ESO introduced flexible chain segments that reduced cohesive energy density and glass transition temperature, thereby effectively improving flexibility and compatibility (Shan et al. 2024). However, previous studies have primarily concentrated on individual performance aspects of EA at specific dosages, such as compatibility mechanisms or aging behavior, and have not systematically investigated the evolution of the multi-physical properties of EA with varying EPS content.

Based on this, the present study established molecular models of EA with varying EPS contents (10, 20, 30, 40, and 50 wt%) and different curing degrees, followed by validation of model reliability. Corresponding EA samples with these EPS contents were prepared and systematically characterized for their glass transition behavior, thermal expansion properties, damping performance, and rheological characteristics. Through MD simulations, we quantitatively analyzed key parameters, including volumetric, thermal, and mechanical properties, to elucidate the evolution of the physical characteristics of EA with increasing EPS content at the molecular level. A comprehensive comparison was conducted to evaluate the consistency between simulation results and experimental data. This research aims to address the current challenge of lacking unified testing methods for evaluating both thermoplastic and thermosetting EA materials. By establishing MD simulation as an effective auxiliary tool for EA material development and design, providing a theoretical foundation for expanding the application diversity of EA and enhancing the longevity of transportation infrastructure. The integrated experimental-simulation approach offers new insights into the composition-structure-property relationships of EA systems across different EPS concentrations.

2. Materials and Methods

2.1 Raw materials

The 60–80 pen grade base binder used in this study was supplied by Sinopec Jinling Petrochemical Co., Ltd. (Nanjing, China), while the self-developed epoxy resin system (EPS) was formulated using epoxy resin, an amine-based curing agent, and a toughening agent. The fundamental properties of these materials were characterized in compliance with the Chinese standards "Technical specification for construction of highway asphalt pavements" (JTG F40-2004) and "Plastics - Determination of tensile properties" (GB/T 1040.1-2018) (State Administration of Market Supervision and Administration 2018; Ministry of Transport of China 2004), with the detailed test results presented in Tables 1 and 2.

Table 1. Fundamental properties of the base binder

Index		Result	Specification
Penetration (25°C,100 g, 5 s)/ 0.1mm		68.6	60–80
Ductility (5 cm/min, 10°C)/ cm		26.5	⩾20
Softening point/ °C		47.4	⩾46
Density (25°C)/ (g/cm^3)		1.035	–
Dynamic viscosity (60°C)		243	⩾180
After RTFOT（163℃, 5h）	Mass loss/ %	-0.4	⩽1.0
	Penetration ratio (25 ℃)/ %	63	⩾61
	Ductility (10 ℃)/ cm	7.0	⩾6

Table 2. Technical specifications of the EPS and EA

Material type	EPS	EA (Base binder: ES= 60:40 wt%)	Specification for EA
Tensile strength/Mpa	8.3	3.6	≥2.0
Elongation at break/%	133.9	241.7	≥100

2.2 Preparation

Considering the balance between cost and performance improvement, the epoxy resin (ES) content in EA typically does not exceed 50 wt% (Sun, Huang, et al. 2023; Sun, Luo, Huang, Hu, et al. 2023). It should be noted that based on preliminary research, modified epoxy resin (MEP) was first obtained by prepolymerizing epoxy resin with a toughening agent at a mass ratio of 100:20 at 150°C for 3 h. The preparation process of EA in this study is shown in Fig. 1. First, the MEP preheated to 60°C was mixed with the curing agent at a mass ratio of 64:36 and stirred at 60°C for 3 minutes. Then, according to the mass ratios of ES to base binder of 10:90, 20:80, 30:70, 40:60 and 50:50, ES was added to the base binder preheated to 160°C and stirred at 160°C for 3 minutes. Finally, the prepared EA was named EA10, EA20, EA30, EA40 and EA50 according to its ES content and cured in a 60°C oven for 4 d.

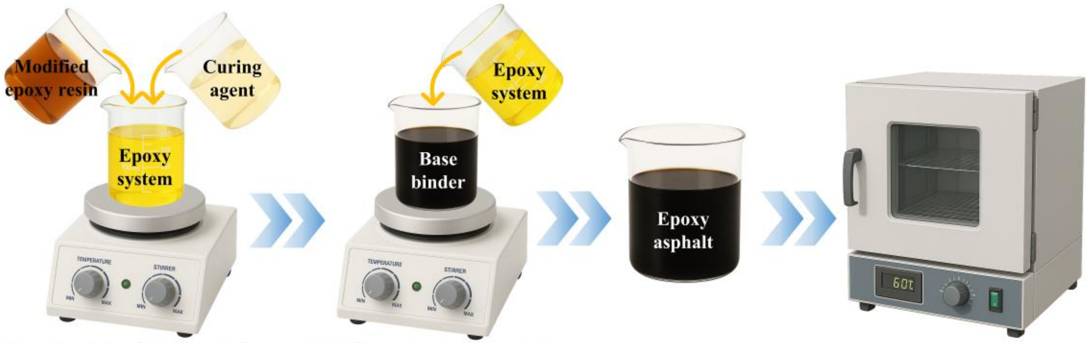

The mass ratio of MEP to curing agent was 64:36, and stirred at 60°C for 3 min.

The ES was added to the asphalt in specific proportions and stirred at 160°C for 3 min.

The obtained EA was placed in an oven at 60°C to cure for 4 d.

Fig. 1. Preparation process of EA

2.3 Test Methods

When the ES content was 10, 20, and 30 wt%, it failed to form a crosslinked network in the EA system. Consequently, EA10, EA20, and EA30 remained thermoplastic materials whose high-temperature rheological properties were evaluated using Dynamic Shear Rheometer (DSR) tests. In contrast, EA40 and EA50 transformed from thermoplastic to thermosetting materials due to ES crosslinking network formation, and their damping properties were characterized through Dynamic Mechanical Analysis (DMA) tests. All EA materials existed in solid state at low temperatures, and their low-temperature rheological properties were examined using Bending Beam Rheometer (BBR) tests.

2.3.1 Differential scanning calorimetry (DSC) test

The glass transition temperature (T_g) of various materials was measured using a NETZSCH DSC214 differential scanning calorimeter. The samples were first heated from -40°C to 100°C at a heating rate of 10 K/min to eliminate thermal history, then cooled back to -40°C, followed by reheating to 100°C at the same rate to obtain the heat flow curves. The testing procedure employed a 60 mL/min nitrogen purge gas flow with an additional 40 mL/min protective gas flow throughout the measurements.

2.3.2 Thermo-mechanical analysis (TMA) test

Thermal mechanical analysis (TMA) was performed on a METTLER TOLEDO TMA/SDTA 2+ analyzer to evaluate EA10, EA20, EA30, EA40, and EA50 samples under a constant stress of 0.01 N with temperature ramping from -40°C to 60°C at 2°C/min. The coefficient of linear thermal expansion (α_{CLTE}) was calculated according to Eq. (1).

$$\alpha_{\mathrm{CLTE}}=\frac{1}{L_0}\times\frac{\Delta L}{\Delta T} \tag{1}$$

where α_{CLTE} represents the coefficient of linear thermal expansion (ppm/°C); L_0 denotes the initial sample length at reference temperature (μm); $\frac{\Delta L}{\Delta T}$ is the slope of the corresponding segment in the TMA curve.

2.3.3 DSR test

In accordance with ASTM D7175 (ASTM International 2020), EA10, EA20, and EA30 samples (Φ25×1 mm) were tested using a NETZSCH Kinexus rotational rheometer. The test parameters included a strain level of 1.25%, frequency of 10 rad/s, and temperature range of 52–100°C. Temperature sweep test results were analyzed to evaluate variations in complex modulus (G), phase angle (δ), and rutting factor ($G/\sin\delta$), thereby characterizing the viscoelastic and rheological properties of different EA.

2.3.4 DMA tyest

Following ASTM D4092 (ASTM International 2013), EA40 and EA50 specimens (35×8×3 mm) were prepared and tested using a TA DMA Q850 instrument in tensile mode. The DMA test conditions included a frequency of 10 Hz, temperature range of -60°C to 100°C, heating rate of 2°C/min, amplitude of 20 μm, and strain level of 0.1% to determine storage modulus (E'), loss modulus (E''), and loss tangent ($\tan \delta$).

2.3.5 BBR test

According to ASTM D6648 (ASTM International 2016), EA specimens (127×12.7×6.35 mm) were prepared and tested using a CANNON TE-BBR SD bending beam rheometer to determine low-temperature creep rate (m) and creep stiffness (S) at -6, -12, and -18°C.

3 Establishment of molecular models

The COMPASS II force field was selected for this study due to its superior accuracy in predicting structures and properties compared to other force fields such as Dreiding and PCFF (Du, Zhu, and Zhang 2021). During the relaxation process, the system was sequentially calculated using NVT and

NPT ensembles, with temperature controlled by the Nosé-Hoover-Langevin (NHL) method and pressure regulated by the Berendsen method. For the stepwise cooling simulation, the NPT ensemble was employed to capture volume changes under constant pressure. To ensure computational accuracy, the minimum edge length of the periodic unit cell was maintained at least twice the cutoff radius. Electrostatic interactions were calculated using the Ewald summation method, while van der Waals interactions were treated with the Atom-based summation approach, both implemented with a cutoff distance of 18.5 Å.

3.1 Molecular modeling of asphalt systems

As a complex mixture system, asphalt presents challenges for fully realistic molecular-level modeling due to its diverse components and intricate interactions. Current modeling approaches primarily include the average molecule method and the assembly method. The average molecule method simplifies the system by constructing representative molecular models, but inevitably neglects certain components and their interactions. In contrast, the assembly method provides more accurate characterization of asphalt composition and intermolecular interactions through multi-component molecular combinations, albeit with higher computational demands (Wang et al. 2025; Nie, Chow, and Lau 2022). This study employs the assembly method to construct asphalt molecular models using Materials Studio software. The development of assembly modeling has progressed from three-component to multi-component systems, with the most representative being the four-component twelve-molecule model proposed by Li and Greenfield. Based on asphalt samples (AAA-1, AAK-1, AAM-1) from the U.S. Strategic Highway Research Program (SHRP), this model classifies asphalt into saturates (non-polar light hydrocarbons), aromatics (low molecular weight hydrocarbons), resins (polar polycyclic compounds), and asphaltenes (highly polar macromolecules), represented by twelve characteristic molecules (D.D. Li and Greenfield 2014). Notably, while the original four-component twelve-molecule model represents a minimized ratio configuration, we proportionally scaled up the molecular quantities to accommodate varying ES content levels and enhance precision in ES dosage control. The final molecular ratios are presented in Table 3.

Table 3. Molecular Composition of the Four-Component Twelve-Molecule Model

Representative Components & Molecules		Molecular Formula	Number of Molecules	Mass Fraction	
Saturates	Squalane	$C_{30}H_{62}$	8	5.187%	11.111%
	Hopane	$C_{35}H_{62}$	8	5.924%	
Aromatics	PHPN	$C_{35}H_{44}$	22	15.683%	31.901%
	DOCHN	$C_{30}H_{46}$	26	16.218%	
Resins	Quinolinohopane	$C_{40}H_{59}N$	8	13.367%	39.737%
	Thioisorenieratane	$C_{38}H_{56}S$	8	6.182%	
	Benzobisbenzothiophene	$C_{18}H_{10}S_2$	30	6.797%	
	Pyridinohopane	$C_{36}H_{57}N$	8	7.030%	
	Trimethylbenzeneoxane	$C_{26}H_{44}O$	10	6.361%	
Asphaltenes	Phenol	$C_{42}H_{54}O$	6	5.291%	17.250%
	Pyrrole	$C_{66}H_{81}N$	4	5.451%	
	Thiophene	$C_{51}H_{62}S$	6	6.508%	

3.2 Molecular modeling of EPS

The EPS system consists of epoxy resin, curing agent, and toughening agent, where both the epoxy resin monomer and toughening agent are polymers with varying repeating units. Due to undetermined polymerization degrees, establishing precise molecular models directly proves challenging. Therefore, the optimal polymerization degree was determined to accurately represent polymer characteristics while maintaining computational efficiency through solubility parameter calculations across varying polymerization degrees (Yu et al. 2021). After constructing molecular models with polymerization degrees ranging from 0 to 15, the geometric optimization and molecular dynamics relaxation were performed to compute their solubility parameters. The optimal polymerization degrees were ultimately determined as 0 for epoxy resin and 10 for the toughening agent. Based on these results, we stoichiometrically converted the actual mass ratios according to different EPS content levels in EA. The specific material ratios adopted for each model are presented in Table 4.

Table 4. Molecular Formulation of EPS and EA Blending Models

Material type	Component	Molecular formula	Molecular weight	Molecule count	Mass fraction	System mass/%
EA10	Epoxy Resin	$C_{21}H_{24}O_4$	340	12	5.63%	10.18%
	Curing Agent	$C_{18}H_{37}N$	267	10	3.68%	
	Toughener	$C_{40}H_{56}N_2O_4$	628	1	0.87%	
EA20	Epoxy Resin	$C_{21}H_{24}O_4$	340	27	11.16%	20.91%
	Curing Agent	$C_{18}H_{37}N$	267	23	7.46%	
	Toughener	$C_{40}H_{56}N_2O_4$	628	3	2.29%	
EA30	Epoxy Resin	$C_{21}H_{24}O_4$	340	45	16.29%	30.71%
	Curing Agent	$C_{18}H_{37}N$	267	39	11.08%	
	Toughener	$C_{40}H_{56}N_2O_4$	628	5	3.34%	
EA40	Epoxy Resin	$C_{21}H_{24}O_4$	340	70	21.83%	40.31%
	Curing Agent	$C_{18}H_{37}N$	267	59	14.45%	
	Toughener	$C_{40}H_{56}N_2O_4$	628	7	4.03%	
EA50	Epoxy Resin	$C_{21}H_{24}O_4$	340	102	26.64%	50.00%
	Curing Agent	$C_{18}H_{37}N$	267	88	18.05%	
	Toughener	$C_{40}H_{56}N_2O_4$	628	11	5.31%	
EPS	Epoxy Resin	$C_{21}H_{24}O_4$	340	45	53.03%	100.00%
	Curing Agent	$C_{18}H_{37}N$	267	39	36.09%	
	Toughener	$C_{40}H_{56}N_2O_4$	628	5	10.88%	

3.3 Molecular modeling of EA

The curing process of EPS is a complex chemical reaction mechanism where epoxy groups first undergo ring-opening reactions with active hydrogen atoms on primary amines, generating hydroxyl groups while converting primary amines to secondary amines, followed by further reaction of another epoxy group with the secondary amine to transform it into a tertiary amine (Sun, Huang, et al. 2023). Although the tertiary amine could theoretically catalyze the etherification between hydroxyl and epoxy groups, practical studies typically consider only the first two reaction stages due to the significant steric hindrance effects of tertiary amines. To ensure simulation accuracy, we implemented a systematic molecular modeling and optimization protocol beginning with geometry optimization of all components using the Forcite module with the Smart algorithm for 20,000 iterations and charge equilibration via the QEq method, followed by construction of amorphous cells at an initial density of 0.1 g/cm³ using the Amorphous Cell module to ensure proper molecular dispersion. The optimization process sequentially included 500 ps NVT ensemble relaxation, 500 ps NPT ensemble equilibrium calculation, supplemented with 5 annealing cycles (200–600 K), and finally obtained stable molecular models through 300 ps NPT simulation as shown in Fig. 2.

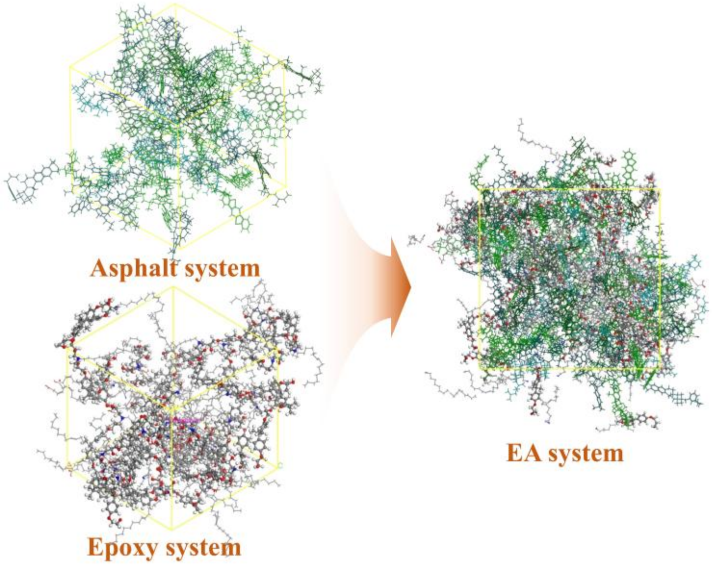

Fig. 2. Construction of molecular model of EA

The crosslinking process of EPS was simulated using a Perl-based crosslinking script, which operates under three fundamental assumptions: equal reactivity of primary and secondary amines, diffusion-dominated crosslinking reactions, and simultaneous progression of all reaction stages (M. Li, Min, Wang, et al. 2023). The implementation procedure involves: (i) identifying reactive sites by marking epoxy carbon atoms (R1) and curing agent nitrogen atoms (R2), while setting target conversion rates and relevant parameters; (ii) initiating the process by searching for qualified reactive atom pairs within an initial cutoff radius of 4.5 Å, followed by epoxy ring-opening to form C–N bonds and subsequent molecular dynamics optimization to verify bond stability; (iii) progressively expanding the crosslinked network through iterative increases of the cutoff radius (0.5 Å increment, up to 15 Å maximum) until achieving the target conversion rate; and (iv) performing geometric optimization and relaxation equilibrium on the resulting crosslinked structure while recording critical parameters including bond lengths, energy values, and molecular fragment distributions, ultimately generating stable system models with specific curing degrees along with corresponding data tables.

To comprehensively investigate the influence of curing degree on material properties, this study established models with curing degrees varying at 10% intervals. It should be noted that in actual computations, minor deviations in curing degree (±2%) may occur due to computational resource limitations and system size constraints, though such variations remain within acceptable margins. The resulting series of models meticulously document the evolution of crosslinked bonds, providing a robust structural foundation for an in-depth understanding of the curing behavior of EA.

3.4 Simulation methods and indicators

3.4.1 Diffusion Coefficient (*D*) and Radial Distribution Function (*RDF*)

Molecular motion is related to its *D*. According to the Einstein relation, the *D* can be defined by Eq. (2) (Huang et al. 2022). The asphalt systems were subjected to 500 ps NPT calculations at different temperatures followed by mean square displacement (*MSD*) analysis. The *D* values of asphalt systems at different temperatures were obtained from the slopes of *MSD* curves. The *RDF* can be used to study the ordering of substances, and its calculation is shown in Eq. (3) (Quan Liu et al. 2023). For molecular simulations, *RDF* calculates the ratio of local particle density to average density in a periodic boundary simulation cell, thereby characterizing the average intermolecular distance within the system, where peak positions indicate the existence of aggregate structures at corresponding distances.

$$D=\frac{1}{6N}\lim_{t\rightarrow\infty}\frac{d}{dt}\langle\left|\overrightarrow{R_{\mathrm{i}}}(t)\text{-}\overrightarrow{R_{\mathrm{i}}}(0)\right|^{2}\rangle \tag{2}$$

$$g(r)=\frac{dN}{\rho 4\pi r^{2}dr} \tag{3}$$

where $\overrightarrow{R_{\mathrm{i}}}(0)$ represents the displacement vector of any atom i in the system at the initial time, $\overrightarrow{R_{\mathrm{i}}}(t)$ denotes the displacement vector of the same atom i after time t, and N is the total number of atoms in the system. ρ indicates the system density (kg/m^3), and r is the interparticle distance (m).

3.4.2 Free Fraction Volume (*FFV*)

Due to the different sizes used when establishing the models, there are initial differences in the free volume among the models. To enable uniform comparison between different models, the *FFV* was employed for description. In the Atom Volumes & Surfaces module, the Connolly surface was selected for construction with a grid spacing set at 0.25 Å. This allowed calculation of the occupied volume and free volume for EA systems with different blending ratios at various curing degrees, and further determination of *FFV*, as calculated by Eq. (4) (L. Luo, Chu, and Fwa 2021).

$$FFV=\frac{V_{\mathrm{f}}}{V_{\mathrm{sp}}}=\frac{V_{\mathrm{sp}}-V_{\mathrm{w}}}{V_{\mathrm{sp}}}=\frac{V_{\mathrm{f}}}{V_{\mathrm{f}}+V_{0}} \tag{4}$$

where, V_{f} represents the free volume; V_{w} denotes the total van der Waals volume of the system; V_{sp} stands for the specific volume (that is, the reciprocal of system density); and V_0 indicates the occupied volume.

Taking the EA30 system as an example, Fig. 3 illustrates the variation of its free volume with curing degree at room temperature. With the increase in curing degree, the number of free-end dangling chain segments in the system gradually decreases as crosslinked network structures develop, resulting in a continuous increase in the system free volume. In the later stages of curing, the increase in *FFV* primarily results from the reorganization and coalescence of existing scattered voids rather than the formation of new ones.

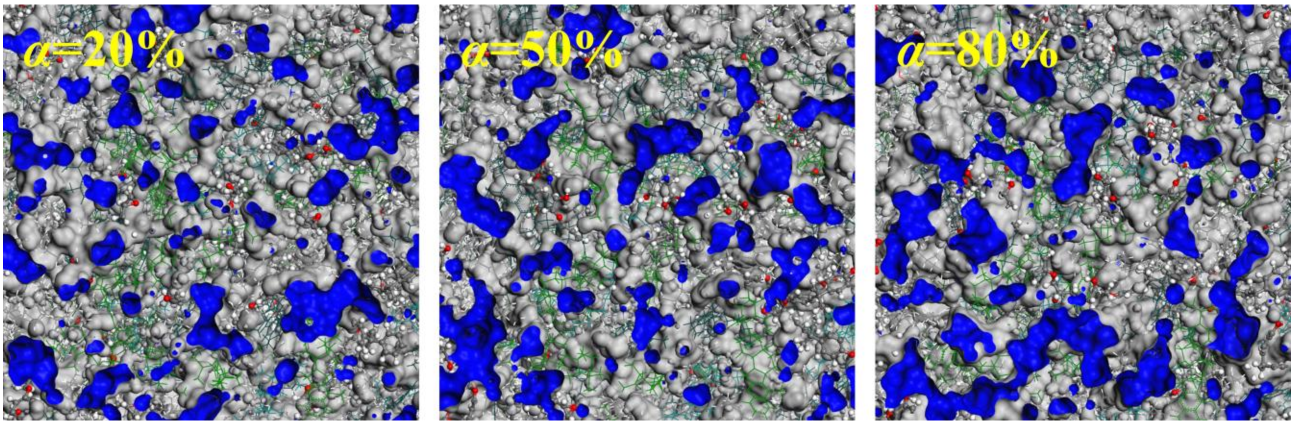

Fig. 3. Free volume change of EA30 model during curing process

3.4.3 Glass Transition Temperature

Materials exhibit distinct volumetric thermal expansion behaviors before and after the glass transition. To characterize this transition, a Perl script was developed to simulate gradual cooling. The models were subjected to a stepwise cooling process from 600 K to 150 K under NPT ensemble conditions at 1 atm, with 100 ps MD calculations performed at 30 K intervals. Stable configurations at each temperature were outputted, and corresponding parameters (density, volume, etc.) were recorded. By plotting temperature-density scatter plots for each system model, a clear inflection point becomes evident. Linear fitting was applied to the data on both sides of this transition, with T_g determined from the intersection point of these fitted lines, as illustrated in Fig. 4.

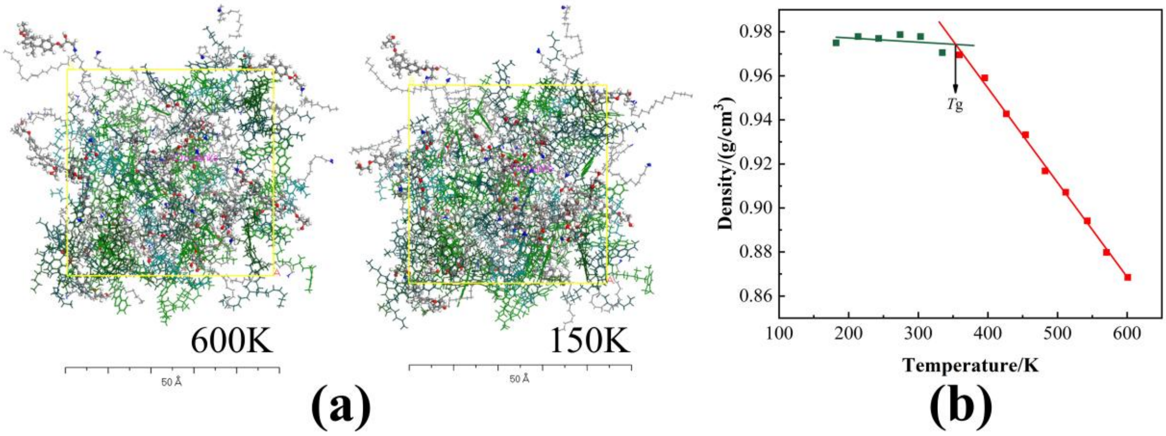

Fig. 4. (a) Volume change of the system during gradual cooling; (b) determination of the T_g

3.4.4 Volume coefficient of thermal expansion（α_{CVTE}）

The volume-temperature curves obtained from the stepwise cooling process allow determination of the α_{CVTE} for different EA samples, as calculated by Eq. (5) (Fang et al. 2024). The density-temperature curves reveal glass transition behavior within the tested temperature range, resulting in an abrupt change in thermal expansion coefficient around T_{g}. Below T_{g}, polymer expansion with increasing temperature arises from amplified molecular vibrations and bond lengthening, representing expansion of the occupied polymer volume characterized by α_{g}. Above T_{g}, thermal energy activates segmental motion, causing unfreezing and expansion of free volume to accommodate chain movement, described by the rubbery-state expansion coefficient α_{r} as defined in Eqs. (6) and (7) (Fedyaeva et al. 2013). Additionally, the free volume expansion coefficient near T_{g} corresponds to the differential between polymer expansion coefficients below and above T_{g} ($\Delta\alpha$), given by Eq. (8).

$$\alpha_{\mathrm{CVTE}}=\frac{1}{V_0}\left(\frac{\partial V}{\partial T}\right)_{\mathrm{P}} \tag{5}$$

$$\alpha_{\mathrm{r}}=\frac{1}{V_{\mathrm{g}}}\left(\frac{\partial V}{\partial T}\right)_{\mathrm{r}} \tag{6}$$

$$\alpha_{\mathrm{g}}=\frac{1}{V_{\mathrm{g}}}\left(\frac{\partial V}{\partial T}\right)_{\mathrm{r}} \tag{7}$$

$$\Delta\alpha = \alpha_{\mathrm{r}} - \alpha_{\mathrm{g}} \tag{8}$$

where, P represents the system pressure, P=1.0×10^5 Pa, V denotes the system volume, T indicates the system temperature, V_0 stands for the system volume at a specific reference temperature (taken as the volume at 150 K in this study), and V_{g} signifies the total volume of the polymer at its glass transition temperature T_{g}.

3.4.5 Damping property

Under the "Mechanical Properties" task, when using the constant strain calculation method, the system is strain-controlled and undergoes a loading cycle from compression to tension according to the input strain amplitude and its gradient, after which corresponding parameters such as modulus are calculated from the mechanical response. Using the energy dissipation before and after the Mechanical Properties calculation as an indicator, the loss factor can be defined as the ratio of the difference in total system energy before and after calculation to the energy before the unloading cycle begins (Sharma et al. 2016). With the strain level set at 0.003, mechanical property calculations were performed at different temperatures for EAs with various blending ratios, and the temperature-dependent variation of their loss factors was determined through energy changes before and after calculations.

3.4.6 Mechanical property

The "Mechanical Properties" task in the Forcite module enables the calculation of various mechanical properties of the system, including Young's modulus (*E*), bulk modulus (*K*), shear modulus (*G*), and Poisson's ratio (*v*), based on the principle of static constant strain method. This method applies small strains to the equilibrated system to induce uniaxial tensile and compressive deformations along the x, y, and z axes, as well as shear deformations in the xy, xz, and yz planes. The system stiffness matrix is then derived from the model response to these applied strains. Within an acceptable error margin, the crosslinked model system established in the calculations can be treated as an isotropic material (Kacar, Peters, and de With 2015), allowing the stiffness matrix to be simplified as shown in Eq. (9).

$$C_{ij}=\begin{bmatrix} \lambda+2\mu & \lambda & \lambda & 0 & 0 & 0 \\ \lambda & \lambda+2\mu & \lambda & 0 & 0 & 0 \\ \lambda & \lambda & \lambda+2\mu & 0 & 0 & 0 \\ 0 & 0 & 0 & \mu & 0 & 0 \\ 0 & 0 & 0 & 0 & \mu & 0 \\ 0 & 0 & 0 & 0 & 0 & \mu \end{bmatrix} \tag{9}$$

The Lamé constants λ and μ obtained from the simplified stiffness matrix enable the calculation of key mechanical properties: *K* characterizing system rigidity, *E* representing fracture strength, *G* indicating material hardness, and *v* (Wiederhorn et al. 2011), as explicitly defined in Eqs. (10)–(13).

$$K=\frac{\mu(3\lambda+2\mu)}{\lambda+\mu} \tag{10}$$

$$E=\lambda+\frac{2}{3}\mu \tag{11}$$

$$G=\mu \tag{12}$$

$$v=\frac{\lambda}{2(\lambda+\mu)} \tag{13}$$

4. Results and discussion

4.1 Model validation

The accuracy of the established EA model was verified through simulations of density for base binder, EA40 and EPS, as well as the *D* and *RDF* of EA40, with results presented in Fig. 5. Fig. 5(a) shows simulated densities of 0.998, 0.987 and 0.967 g/cm^3 for base binder, EA40 and EPS respectively. Compared with measured values of 1.035 g/cm^3 (base binder, Table 1) and 1.012 g/cm^3 (EPS), these represent deviations of 3.6% and 4.4%, primarily arising from simplification-induced omission of heavy components in modeling. Results in Fig. 5(b) demonstrate diffusion coefficients of 2.68×10^{-6}, 3.10×10^{-6} and 8.17×10^{-6} cm^2/s for the asphalt system across tested temperatures, all lower than the 2×10^{-6} cm^2/s value obtained by Schmets et al. through inelastic neutron scattering experiments at 553.15 K, confirming good consistency between modeled and actual material diffusion behaviors. Fig. 5(c) reveals multiple peaks in the intermolecular *RDF* curve within 0 Å<r<4 Å, indicating significantly higher probability of reference particle appearance at these distances compared to others, which demonstrates certain regularity in adjacent atomic arrangement with peak positions suggesting potential aggregate structures. In contrast, the *RDF* stabilizes around 1 when r exceeds 4 Å. For crystalline materials exhibiting long-range ordered arrangements where particles remain regularly distributed even at infinite distances, *RDF* should display long-range peaks, whereas non-crystalline materials typically only show short-range peaks (Shokuhfar and Arab 2013). These results prove the established system model possesses a non-crystalline structure with long-range disorder and short-range order, matching real material characteristics. The intramolecular *RDF* shows rapid growth within 0 Å<r<7 Å before gradually approaching 1 when r exceeds 7 Å, with hydrogen bonding typically occurring at 2.6–3.1 Å and van der Waals interactions dominating beyond 3.1 Å, confirming van der Waals forces as the primary interactions in the system.

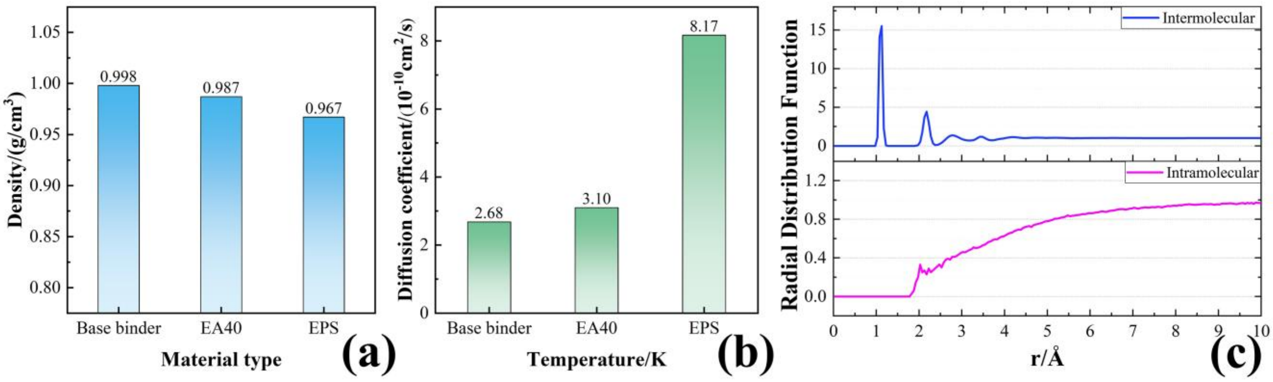

Fig. 5. (a) density; (b) diffusion coefficient; (c) radial distribution function

4.2 FFV

Based on MD simulation results, a systematic analysis was conducted on the free volume characteristics of different EA systems. Fig. 6(a) shows the evolution of *FFV* with curing degree for each system. Overall, the *FFV* of EA increases with increasing curing degree. When the content increases from 10 to 30 wt%, the *FFV* continues to decrease; however, when the content exceeds 30 wt%, the EA system exhibits expansion behavior, with *FFV* higher than that of EA10 and EA20. The results indicate that within the considered content range of 10–50 wt%, there exists an optimal EPS content around 30 wt% where the material exhibits the densest microstructure, as reflected by *FFV* characteristics. As shown in Fig. 6(b), further temperature-variable analysis reveals that all EA systems display characteristic *FFV*-temperature curves, where *FFV* first decreases and then increases with rising temperature, showing distinct inflection points in the 270–300 K range. Notably, the temperature corresponding to the inflection point shows an increasing trend with higher EPS content. According to free volume theory, polymer chain segments are frozen and cannot move freely in the glassy state, while the material volume becomes more sensitive to temperature changes in the rubbery state. Therefore, the T_g serves as the critical point for *FFV* changes in the system. Specifically, below T_g, an increase in temperature affects only the molecular vibration amplitude and bond length, indicating that the volume change of the polymer arises solely from the expansion of occupied volume. As shown in Eq. (4), this leads to a continuous decrease in *FFV*. Above T_g, with increasing temperature, chain segment movement becomes more active, and the expansion rate of free volume exceeds that of occupied volume, resulting in an increase in material *FFV*. Consequently, the inflection point in the *FFV*-temperature curve can serve as a basis for determining the T_g of the material.

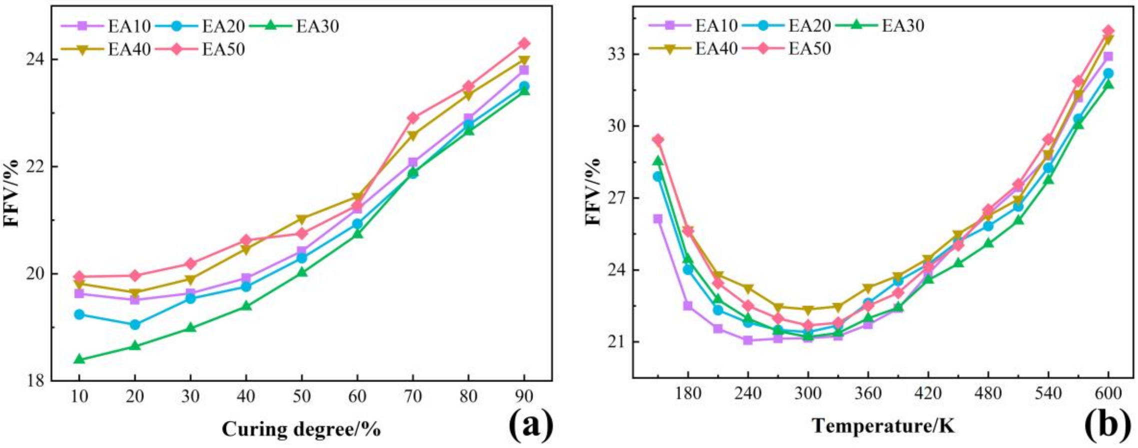

Fig. 6. Simulation results of *FFV* with different EA:

(a) variation with curing degree; (b) variation with temperature

4.2.2 Glass transition temperature

The glass transition behavior of EA systems was analyzed through combined DSC tests and MD simulations. The DSC test results presented in Fig. 7(a) indicate the T_g of EPS measures 21.7°C, markedly higher than the 8.0°C observed for base binder. With EPS content increasing from 10 to 50 wt%, the system T_g demonstrates a monotonic upward trend, confirming EPS incorporation effectively enhances material heat resistance while diminishing low-temperature applicability. MD simulation results displayed in Fig. 7(b) exhibit excellent agreement with experimental data, consistently showing elevated T_g values corresponding to higher EPS content. At molecular scale, key factors governing T_g principally involve molecular chain flexibility and cohesive energy density (Xu and Freed 2014). The crosslinked network structure characteristic of EPS reduces molecular chain flexibility while simultaneously increasing system cohesive energy density, consequently restricting chain segment mobility. As the curing process further improves internal structural compactness, thermodynamic principles dictate material T_g varies with crosslinking degree and displays temperature dependence, thus necessitating investigation into the T_g-curing degree relationship for each EA.

The T_g transition of the system at different curing degrees can be fitted using either the DiBenedetto equation or the Venditti-Gillham equation (Estridge 2018; C. Li et al. 2012), as shown in Eqs. (14) and (15).

$$\frac{T_g - T_g^0}{T_g^\infty - T_g^0} = \frac{\lambda\xi}{1-(1-\lambda)\xi} \tag{14}$$

$$\frac{\ln(T_g) - \ln(T_g^0)}{\ln(T_g^\infty) - \ln(T_g^0)} = \frac{\lambda\xi}{1-(1-\lambda)\xi} \tag{15}$$

where,T_g^0、T_g、T_g^∞ represent the T_g at conversion rates of 0, ξ, and 1, respectively (K); λ is an adjustable parameter describing nonlinear relationships, numerically equal to the ratio of heat capacity step changes between fully cured and uncured systems at their respective T_g values, that is, $\lambda = \frac{\Delta c_{p\infty}}{\Delta c_{p0}}$.

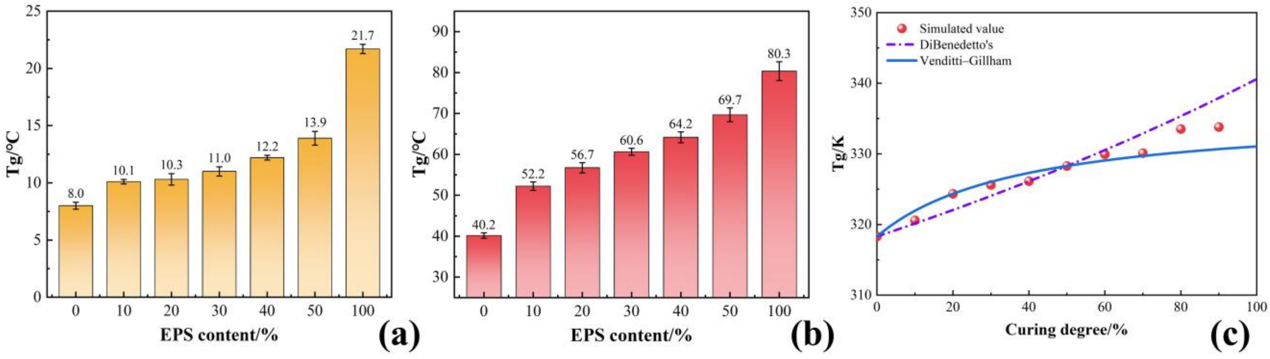

Fig. 7. (a) T_g results based on DSC tests; (b) T_g results based on MD simulations; (c) T_g values at different curing degrees of EA30 and model fitting.

Taking the EA30 system as an example, the gradual cooling script was executed for models at different curing degrees to obtain the corresponding T_g values, with the variation of T_g during the curing process shown in Fig. 7(c). The T_g of the EA30 system exhibited nonlinear growth with increasing curing degree, and the Venditti-Gillham model (R^2=0.98) described this variation more accurately compared to the DiBenedetto model (R^2=0.92). From Eqs. (14) and (15), the derived parameters were T_g^{∞}=340.60 K, λ=0.81 and T_g^{∞}=331.05 K, λ=3.67 respectively, demonstrating that the Venditti-Gillham model provided better fitting results for this system.

A comparison between experimental and simulated values in Figs. 8(a) and 8(b) reveals discrepancies in T_g measurements, primarily attributable to the vastly different cooling rates employed: the simulation utilized an ultra-fast rate of 30 K/100 ps (3×10^{-1} K/ps) at picosecond scale, whereas experiments employed 20 K/min (3.33×10^{-13} K/ps). This significant temporal scale difference induces pronounced thermal inertia effects, creating spatiotemporal misalignment between phase transitions and temperature changes that manifests as hysteresis in glass transition behavior. The WLF equation predicts a 3–5 K increase in Tg per order of magnitude cooling rate acceleration (Mohammadi and Davoodi 2017; Williams, Landel, and Ferry 1955), depending on polymer characteristics. Consequently, the rate differential would account for 36–60 K variation between simulated and experimental values, consistent with observed data. These findings confirm that MD simulations maintain strong consistency with experimental T_g trends despite quantitative offsets, validating their utility for investigating the glass transition behavior of the EA as an alternative to conventional DSC testing, though requiring appropriate correction factors. This approach provides crucial theoretical guidance for EA material design and applications.

4.2.3 Coefficient of thermal expansion

Taking EA30 as an example, the coefficients of thermal expansion before and after the glass transition were calculated using Eqs. (6) and (7) respectively, with the results shown in Fig. 8. It can be observed that the α_{CVTE} of the EA30 increases nearly fourfold upon transitioning from the glassy state to the rubbery state, while both α_{g} and α_{r} decrease with increasing curing degree, with this declining trend becoming particularly significant when the system curing degree reaches approximately 40%. The results demonstrate that the crosslinked network structure formed during the curing process of EA restricts segmental motion within the system while simultaneously suppressing its thermal expansion behavior.

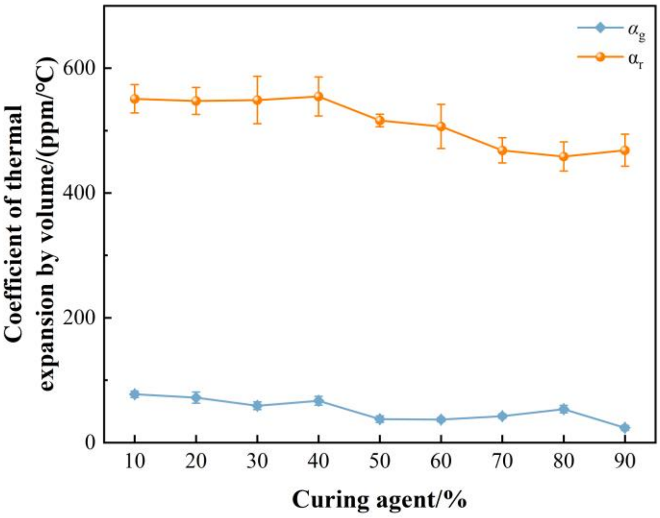

Fig. 8. α_{CVTE} of EA30 at different curing degrees

Assuming the material is an isotropic homogeneous body, the relationship between linear thermal expansion coefficient and volumetric thermal expansion coefficient is $\alpha_{CLTE}=\frac{1}{3}\alpha_{CVTE}$ (Karch 2014). It should be noted that EA10, EA20, and EA30 undergo a solid-to-liquid transition upon temperature increase, making TMA testing unfeasible for these materials. Therefore, TMA tests were conducted only on EA40 and EA50. The simulated α_{CVTE} was converted toα_{CLTE} and compiled with TMA test results in Table 5. As EPS content increases, the α_{g} shows limited growth while α_{r} demonstrates more significant increase, consequently leading to higher $\Delta\alpha$ values. Furthermore, the close agreement between simulated and experimental values for EA40 and EA50 confirms the good applicability of the MD simulation and potential as an experimental alternative for evaluating thermal expansion coefficients. The distinct macroscopic properties of EA in rubbery and glassy states, reflected in the difference between α_g and α_r, indicate that larger $\Delta\alpha$ values correspond to greater disparity in molecular mobility before and after glass transition, representing larger free volume available for network chain movement. Thus, $\Delta\alpha$ during the glass transition can reflect the *FFV* of the material and may be regarded as the thermal expansion coefficient of free volume within the system.

Table 5. α_{CLTE} of EA at different contents

Material type	α_{CLTE} (simulated value)/(ppm/°C)			α_{CLTE} (test value)/(ppm/°C)		
	α_g	α_r	$\Delta\alpha$	α_g	α_r	$\Delta\alpha$
EA10	55.9	90.4	34.5	–	–	–
EA20	62.2	118.5	56.3	–	–	–
EA30	67.3	135.2	67.9	–	–	–
EA40	68.6	139.9	71.3	–	134.31	–
EA50	79.1	156.2	77.1	–	173.43	–

It is noteworthy that numerous studies on amine-cured epoxy resins have demonstrated that both density and *K* decrease with reduced T_g, a phenomenon typically explained by volumetric characteristics where *FFV* diminishes with increasing crosslinking density (Koike and Ishizaki 1999; Montazeri, Pourshamsian, and Riazian 2012). The glassy state of amorphous materials can be considered an iso-free-volume state, exhibiting an *FFV* of approximately 0.025 at T_g. The *FFV* of crosslinked epoxy networks can be determined using the C_1 and C_2 parameters of the WLF equation, calculated through Eqs. (16) and (17) according to free volume theory (Montazeri, Pourshamsian, and Riazian 2012). When T_g is used as the reference temperature, C_1=17.44 and C_2=51.6. The *FFV* of the material at T_g (f_g) is calculated as shown in Eq. (18), with results for all EA systems compiled in Table 6. The data reveal that increasing EPS content elevates of the the system, potentially attributable to initial defects like voids in the crosslinked network and the presence of toughening agents in the composition. Furthermore, f_g demonstrates calculation trends similar to *FFV*, confirming their strong correlation.

$$C_1=\frac{B}{2.303f_g} \tag{16}$$

$$C_2=\frac{f_g}{\Delta\alpha} \tag{17}$$

$$f_g=\sqrt{\frac{B\Delta\alpha\frac{C_2}{C_1}}{2.303}} \tag{18}$$

where, B represents a coefficient that is approximately equal to 1 for nearly all materials; f_g denotes the free volume fraction of the material at T_g (%); α stands for the thermal expansion coefficient (ppm/°C); and $\Delta\alpha$ indicates the difference in thermal expansion coefficients before and after the transition (ppm/°C).

Table 6. f_g of each sample obtained from the coefficient of thermal expansion

Material type	EA10	EA20	EA30	EA40	EA50
f_g	6.66	8.50	9.34	9.57	9.95

4.3 Damping property

The temperature-dependent characteristics of E', E'', and tan δ for all samples at 10 Hz frequency are shown in Figs. 10(a) and 10(b). The results reveal that E' exhibits a gradual decline in the -60°C to -30°C range, followed by a significant reduction between -30°C and 20°C, eventually approaching zero above 40°C. E'' demonstrates an increasing trend from -50°C to -10°C, then decreases between 0°C and 40°C, with a distinct peak appearing between -10°C and 0°C. Tan δ shows continuous growth from -60°C to 45°C, subsequently decreasing from 45°C to 100°C, while displaying a prominent peak between 40°C and 50°C. Regarding the effect of EPS content, systematic variations are observed with increasing content: E' shows substantial enhancement, E'' decreases, and the tan δ peak exhibits a declining trend, accompanied by high-temperature shifts in both E'' and tan δ peaks. Specifically, for EA40 and EA50 samples, higher EPS content leads to reduced tan δ peak values, indicating decreased energy dissipation from intermolecular friction in polymer chains. This phenomenon suggests reduced resistance to segmental motion under external forces, manifesting as increased α_{CLTE} during temperature variations.

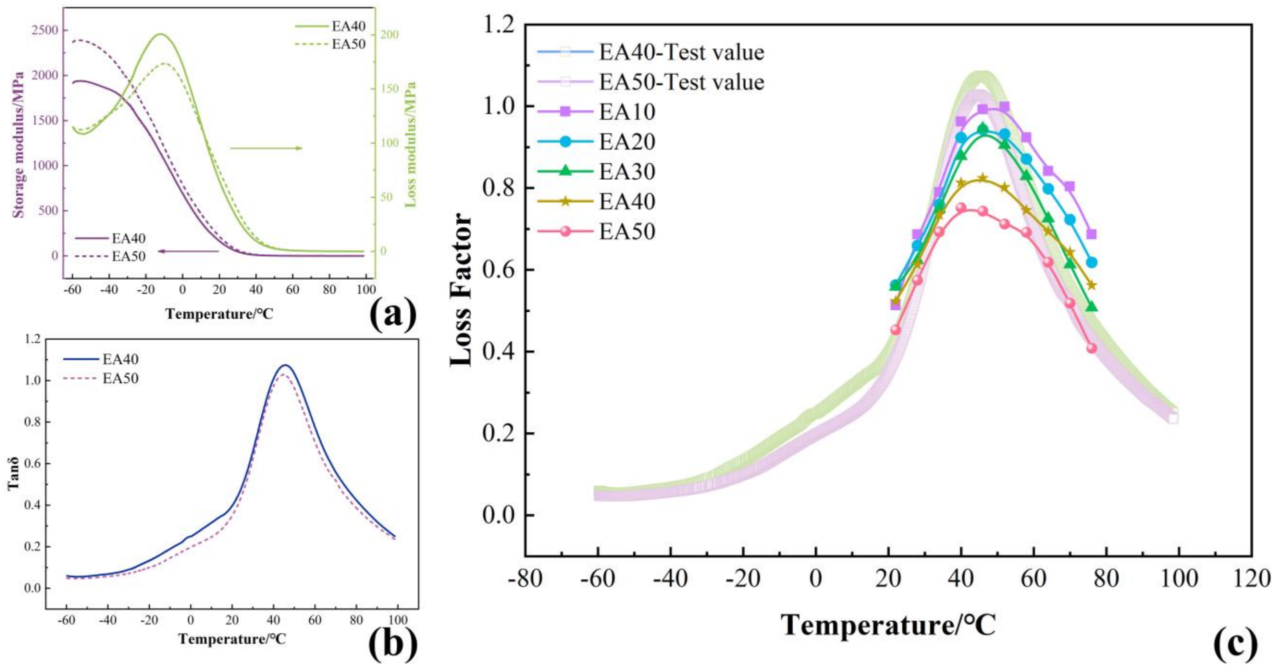

Fig. 9. DMA test and MD simulation results for EA: (a) E' and E''; (b) tanδ; (c) loss factor

It is noteworthy that all samples exhibit only a single-step transition in their E'-temperature curves, and the tan δ curves display just one relaxation peak without the dual-peak characteristics indicative of phase separation behavior, demonstrating satisfactory compatibility between EPS and asphalt. Furthermore, distinct differences exist in the peak profiles of the tan δ curves. Generally, a larger full width at half maximum (FWHM) suggests a more prolonged and complex glass transition process, reflecting heterogeneity in the crosslinked network system. Comparing EA40 and EA50 samples, EA50 demonstrates a narrower FWHM, confirming better uniformity in its crosslinked network structure, a finding consistent with previous research (S. Luo et al. 2022).

The damping performance of materials was evaluated through systematic analysis of three key parameters: the tan δ peak value ($\tan\delta_{\max}$), effective damping temperature range (ΔT), and curve integral area (*TA*) (H. Li et al. 2020), with detailed data presented in Table 7. Results demonstrate that both EA40 and EA50 exhibit outstanding damping properties while showing distinct differences in critical parameters. EA40 reaches its tan$\delta_{\max}$ of 1.077 at 45.54°C, slightly higher than the peak value of 1.031 shown by EA50 at 44.62°C, indicating both materials achieve optimal damping effectiveness within the 44–46°C range. More notably, EA40 demonstrates a ΔT of 84.32°C, approximately 11.3°C wider than the 73.02°C range of EA50, representing a broader effective damping temperature domain. Furthermore, the *TA* value of 53.21°C for EA40 shows 15.6% improvement compared to 46.03°C for EA50, further confirming superior comprehensive damping performance. This phenomenon occurs because both EA40 and EA50 belong to thermosetting materials where EPS forms crosslinked network structures, increased EPS content enhances chain segment mobility, consequently reducing damping performance.

Table 7. Characterization of damping properties of EA at different contents

Material type	tan$\delta_{\max}$	ΔT/°C	*TA*/°C
EA40	1.077 (45.54°C)	84.32 (7.92~92.24)	53.21
EA50	1.031 (44.62°C)	73.02 (16.49~89.51)	46.03

Fig. 9(c) presents the loss factors of different EA systems obtained through MD simulations. The temperature range for MD simulations was set at 22–76°C based on DMA test results. All EA systems exhibit characteristic non-monotonic variation in loss factors, showing an initial increase followed by decrease during heating, with peak values appearing within the 30–60°C range. Regarding EPS content effects, increasing EPS content leads to distinct high-temperature shifts in peak loss factor temperatures while narrowing the peak temperature range. The MD simulation results demonstrate consistent trends with experimental values, successfully verifying the patterns for thermoplastic EA10, EA20 and EA30 systems that could not be tested experimentally. However, the simulated peak loss factor values appear lower than experimental measurements. This discrepancy primarily originates from differences between simulation loading conditions and DMA test parameters, including incomplete matching of strain amplitude and frequency characteristics.

4.4 Mechanical properties

The DSR test results are presented in Fig. 10(a). The rutting factor ($G^*/\sin\delta$) of EA increases with higher EPS content, demonstrating that EPS incorporation effectively enhances the high-temperature shear deformation resistance of the binder (Sun et al. 2022). Notably, EA30 shows a substantial jump compared to EA10 and EA20, indicating an impending phase transition at 30 wt% EPS content, which aligns with previous research findings (S. Luo et al. 2022). The BBR results in Figs. 11(b) and 11(c) reveal that the S of EA increases with EPS content, reflecting intensified physical hardening at low temperatures and suggesting compromised low-temperature cracking resistance. Simultaneously, the m of EA progressively decreases, with the most pronounced reduction (up to 59%) occurring between EA30 and EA40. This phenomenon primarily stems from the phase transition affecting the material properties occurs between 30 and 40 wt% EPS contents, where a three-dimensional crosslinked network structure with EPS as the continuous phase gradually forms. This structure significantly diminishes the viscous characteristics of the binder, leading to markedly weakened low-temperature creep capability.

For the EA30 system, Fig. 11(a) presents the MD simulation results of K, E, and G at room temperature (23°C). The K, E, and G of EA30 all show positive correlation with curing degree while exhibiting distinct stage characteristics. Specifically, each modulus demonstrates fluctuating but gradual growth during early curing stages, with significant enhancement only appearing after 80% curing degree, indicating delayed strength development during the curing process. At 90% curing degree, the model achieves maximum values of 3.85 GPa (K), 3.52 GPa (E), and 1.67 GPa (G). Notably, orders-of-magnitude discrepancies exist between MD simulation results and experimental measurements. This systematic deviation primarily originates from inherent force field limitations - the cutoff radius in energy calculations being smaller than model dimensions, combined with artificially reduced simulation scales and absence of complex initial defects in MD models.

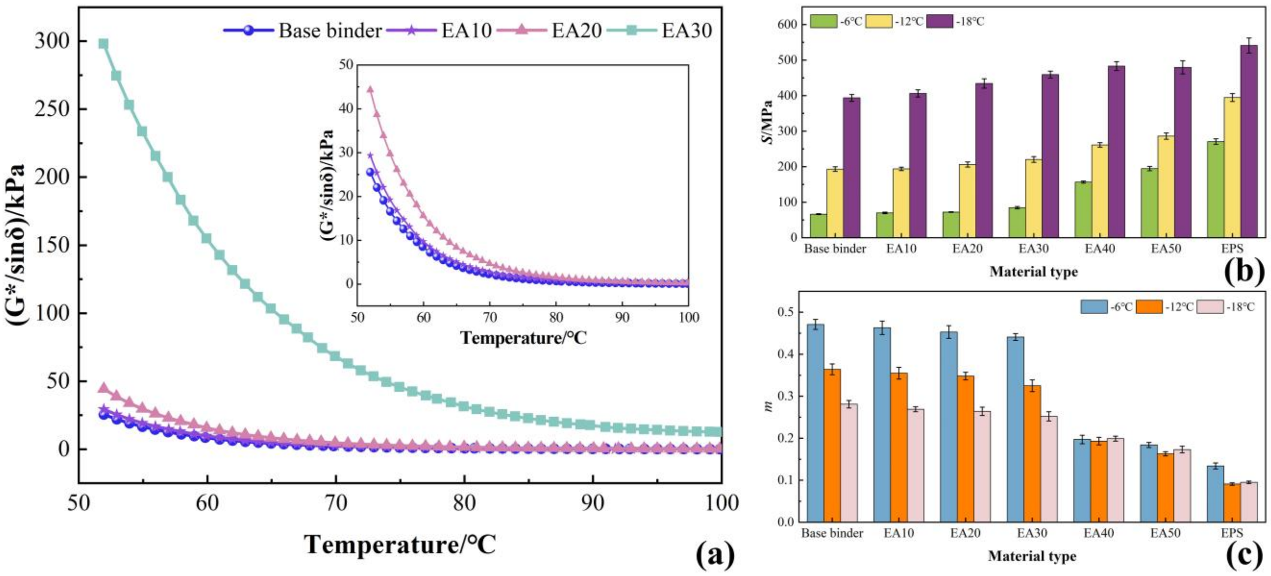

Fig. 10. (a) DSR test results; (b) and (c) BBR test results

Under different environmental conditions, EA demonstrates varying mechanical properties with distinct temperature sensitivity. To investigate its high- and low-temperature performance, two temperature ranges were established based on actual pavement service temperatures and ASTM performance grade (PG) standards: high-temperature (64, 70, 76, and 82°C) and low-temperature (-6, -12, -18, and -24°C) conditions. MD simulations were performed to evaluate mechanical properties of the EA across these temperatures (ASTM International 2023), with results shown in Figs. 12(b) and 12(c). Under high temperatures, all systems exhibited decreasing *K*, *E*, and *G* values with rising temperature. Regarding EPS content effects, each modulus increased significantly with higher EPS content, particularly showing marked enhancements between EA20–EA30 and EA30–EA40. This confirms that the three-dimensional crosslinked network formed by EPS effectively restricts molecular chain segment mobility within the material, thereby substantially improving structural stability and mechanical performance at elevated temperatures. Under low-temperature conditions, all EA moduli displayed systematic increases with temperature reduction, exhibiting typical low-temperature hardening characteristics. These results macroscopically reflect reduced flexibility and enhanced brittleness of the material in cold environments, showing consistency with BBR test findings.

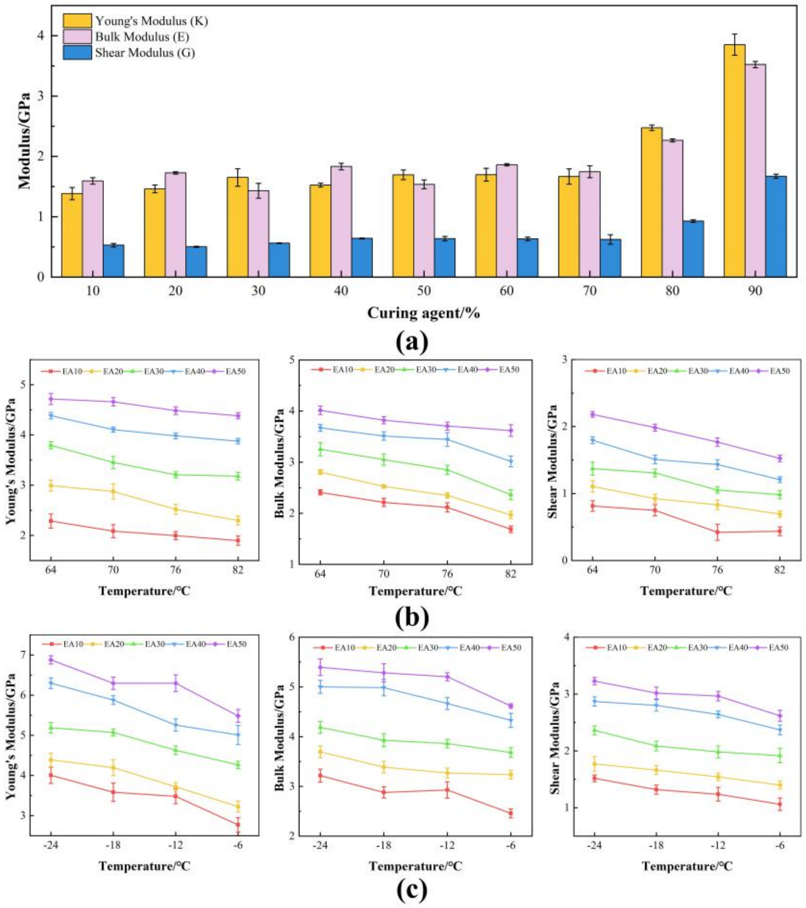

Fig. 11. (a) MD simulation results of mechanical properties of EA30 at 23°C; (b) MD simulation results of mechanical properties of EA at high temperatures, (c) MD simulation results of mechanical properties of EA at low temperatures

The *v* of polymers in the glassy state typically ranges between 0.3–0.46 (Qingqing Liu 2020). As demonstrated in Fig. 12(a), all EA systems show *v* values within this theoretical range, further verifying simulation accuracy. The E/G ratio represents a critical indicator for evaluating material brittleness-ductility transitions. Following classical mechanics theory, materials display brittle characteristics when *E*/*G* falls below 1.75, while maintaining ductile behavior above this threshold. Fig. 12(b) presents MD simulation results of EA systems across various low temperatures. All EA systems exhibit decreasing *E*/*G* ratios with temperature reduction, indicating progressive ductility loss during cooling. Under extreme low-temperature conditions (-24°C), high-EPS-content systems including EA40 and EA50 demonstrate *E*/*G* ratios below 1.75, showing distinct brittle characteristics, while other systems retain ductile behavior with ratios above the critical value. These results confirm that increased EPS content promotes brittle-ductile transitions in EA materials at low temperatures, consequently elevating risks of brittle fracture.

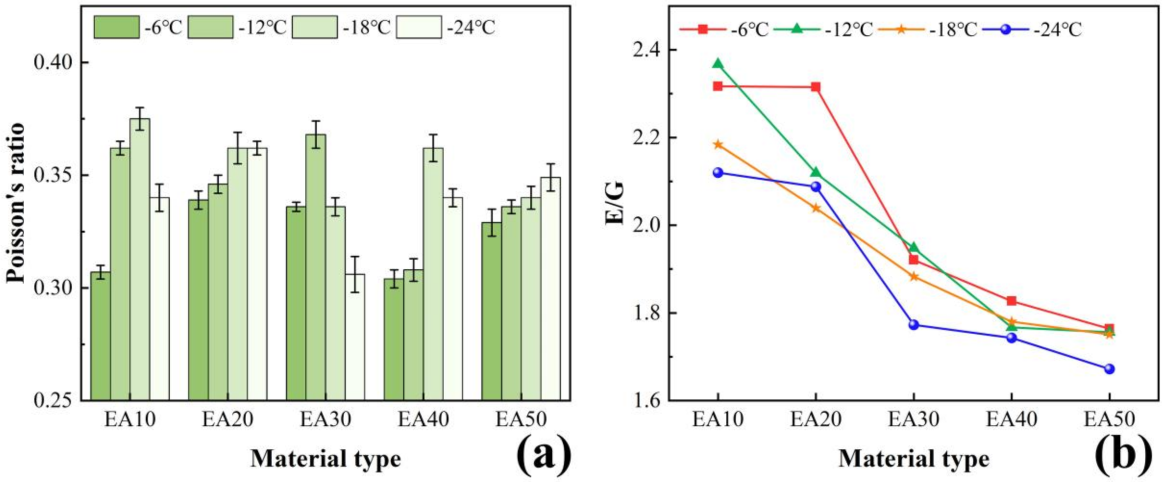

Fig. 12. (a) Poisson's ratio MD simulation results for EA; (b) *E*/*G*

5. Conclusions

This study systematically investigated the influence mechanism of EPS content on EA physical properties through combined MD simulations and experimental methods. The key parameters such as thermal, volumetric and modulus properties were calculated by MD simulation and verified with a series of experimental test results, and the correlation between simulation and experiment was analyzed. The main conclusions are as follows:

a) The volumetric characteristics and glass transition behavior of EA systems exhibit significant dependence on both EPS content and curing degree. The material structure reaches optimal density near 30 wt% EPS content. Although increasing EPS content enhances thermal resistance, the high thermal expansion coefficient of EPS adversely affects volumetric stability, with EA demonstrating significantly higher expansion coefficients in the rubbery state than in the glassy state.

b) EA40 outperforms EA50 in damping peak value, effective temperature range and energy dissipation capacity, indicating better balance between mechanical and damping properties. The consistency between MD simulations and experimental data verifies material homogeneity while revealing that higher EPS content promotes denser crosslinked networks at the expense of damping performance.

c) Elevated EPS content markedly improves high-temperature performance but gradually reduces low-temperature flexibility, inducing a ductile-to-brittle transition. Near 30 wt% content, the material transitions from asphalt-dominated thermoplasticity to crosslink network-dominated thermosetting behavior, causing abrupt improvement in high-temperature mechanical properties while accelerating low-temperature brittleness. MD simulations confirm this temperature sensitivity despite numerical discrepancies with experiments.

d) MD simulations effectively overcome difficulties in testing methods and evaluation between thermoplastic and thermosetting EA, revealing continuous evolution of physical properties across EPS contents. Although numerical differences exist, consistent trends validate the reliability of simulation. As an efficient complementary tool, MD can replace time-consuming experimental tests during preliminary EA formulation screening, significantly reducing R&D costs and cycles while improving development efficiency.

e) Future research should employ multiscale simulations to elucidate phase transition mechanisms at critical EPS contents and their synergistic effects on material performance. Simultaneously, enhancing the engineering applicability and accuracy of MD simulations will promote efficient material design and diversified EA applications.

Acknowledgements:

This work was undertaken with funding from the National Natural Science Foundation of China (No. 52278445), the Major Science and Technology Project of Nanjing (No. 202209012), the Carbon Peak and Carbon Neutrality Science and Technology Innovation Special Funds of Jiangsu Province (No. BE2022615), and the SEU Innovation Capability Enhancement Plan for Doctoral Students (No. CXJH_SEU 24041). Moreover, the author would like to express their gratitude to the China Scholarship Council (CSC) for funding this research.

Declaration of Interest statement

The authors declare that they have no known competing financial interests or personal relationships that could have appeared to influence the work reported in this paper.

References

Almeida, Arminda, and Luís Picado-Santos. 2022. "Asphalt Road Pavements to Address Climate Change Challenges—An Overview." Applied Sciences 12 (24): 12515.

Bocci, Edoardo, and Francesco Canestrari. 2012. "Analysis of structural compatibility at interface between asphalt concrete pavements and orthotropic steel deck surfaces." Transportation Research Record 2293 (1): 1-7.

Chen, Xiang, Yan Chen, Tao Ma, Linhao Gu, and Shuang Shi. 2024. "Study on the performances of epoxy asphalt binders influenced by the dosage of epoxy resin and its application to steel bridge deck pavement." Construction and Building Materials 432: 136683.

Cheng, Peifeng, Zexin Fan, Xiule Chen, Qichao Gao, and Yiming Li. 2025. "Study on the compatibility mechanism of epoxy asphalt based on molecular dynamics simulations." Chemical Physics Letters: 142194.

Ministry of Transport of China. 2004. Technical Specification for Construction of Highway Asphalt Pavements. JTG F40-2004. Beijing: China Communications Press.

Du, Zhao, Xingyi Zhu, and Yuqing Zhang. 2021. "Diffusive Dynamics and Structural Organization of Moisture in Asphaltic Materials Based on Molecular Dynamics Simulation." Journal of Materials in Civil Engineering 33 (1): 04020403.

Estridge, Carla E. 2018. "The effects of competitive primary and secondary amine reactivity on the structural evolution and properties of an epoxy thermoset resin during cure: A molecular dynamics study." Polymer 141: 12-20.

Fang, Yongwei, Yingying Pang, Jiandong Zhang, Yihan Nie, and Hongquan Lu. 2024. "Glass transition temperature of asphalt binder based on atomistic scale simulation." Frontiers in Materials 11: 1485669.

Fedyaeva, ON, AA Vostrikov, M Ya Sokol, and NI Fedorova. 2013. "Hydrogenation of bitumen in supercritical water flow and the effect of zinc addition." Russian Journal of Physical Chemistry B 7: 820-828.

Huang, Ting, Zengping Zhang, Li Wang, Jia Sun, Zhaofei Wang, Hao Liu, and Liqi Chen. 2022. "Study on the compatibility between polyurethane and asphalt based on experiment and molecular dynamics simulation." Case Studies in Construction Materials 17: e01424.

ASTM International. 2013. Standard Terminology for Plastics: Dynamic Mechanical Properties. ASTM D4092-07. West Conshohocken: PA.

ASTM International. 2016. Standard Test Method for Determining the Flexural Creep Stiffness of Asphalt Binder Using the Bending Beam Rheometer. ASTM D6648-08. West Conshohocken: PA.

ASTM International. 2020. Standard Test Method for Determining the Rheological Properties of Asphalt Binder Using a Dynamic Shear Rheometer. ASTM D7175-15. West Conshohocken: PA.

ASTM International. 2023. Standard Specification for Performance-Graded Asphalt Binder. ASTM D6373-23. West Conshohocken: PA.

Jiang, Wei, Dongdong Yuan, Chengwei Xing, Bowen Zhang, Jingjing Xiao, Teng Wang, and Wangjie Wu. 2023. "Experimental study of epoxy asphalt binder and porous epoxy asphalt concrete." Journal of Cleaner Production 420: 138373.

Kacar, Gokhan, Elias AJF Peters, and Gijsbertus de With. 2015. "Multi-scale simulations for predicting material properties of a cross-linked polymer." Computational Materials Science 102: 68-77.

Karch, Christian. 2014. "Micromechanical analysis of thermal expansion coefficients." Modeling and Numerical Simulation of Material Science 2014.

Koike, Tsuneo, and Noritoshi Ishizaki. 1999. "Free volume and dipole mobility in an epoxide oligomer before crosslinking." Journal of applied polymer science 71 (2): 207-214.

Li, Chunyu, Grigori A Medvedev, Eun-Woong Lee, Jaewoo Kim, James M Caruthers, and Alejandro Strachan. 2012. "Molecular dynamics simulations and experimental studies of the thermomechanical response of an epoxy thermoset polymer." Polymer 53 (19): 4222-4230.

Li, Derek D, and Michael L Greenfield. 2014. "Chemical compositions of improved model asphalt systems for molecular simulations." Fuel 115: 347-356.

Li, Huawei, Wei Wei, Chao Zhang, Feifan Xu, Xin Li, Peng Jing, Quanyao Zhu, Qingjun Ding, and Boxiang Yan. 2020. "Hot mixing behavior and curing process of epoxy asphalt." Journal of Wuhan University of Technology-Mater. Sci. Ed. 35 (3): 605-610.

Li, Mingyue, Zhaohui Min, Han Ouyang, Fei Chen, and Wei Huang. 2023. "The effect of composite curing agent ratio on the photooxidative aging behavior of epoxy asphalt based on molecular dynamics simulation." Construction and Building Materials 409: 134157.

Li, Mingyue, Zhaohui Min, Qichang Wang, Wei Huang, and Zhiyong Shi. 2023. "Influence of curing agent ratio, asphalt content and crosslinking degree on the compatibility and component distribution of epoxy asphalt in compound curing agent system." International Journal of Pavement Engineering 24 (2): 2136375.

Li, Rong, Jianjun Wu, Hao Liu, Ziyou Gao, Huijun Sun, Rui Ding, and Tieqiao Tang. 2019. "Crowded urban traffic: co-evolution among land development, population, roads and vehicle ownership." Nonlinear Dynamics 95 (4): 2783-2795.

Liu, Hao, Zengping Zhang, Youxin Zhu, Jia Sun, Li Wang, Ting Huang, and Liqi Chen. 2022. "Modification of asphalt using polyurethanes synthesized with different isocyanates." Construction and Building Materials 327: 126959.

Liu, Qingqing. 2020. "Molecular dynamics study on the tensile and friction properties of Ti3C2TX mycene/epoxy composites." North Central University.

Liu, Quan, Ruiyu Fang, Jiantao Wu, Wenhao Cha, and Pengfei Liu. 2023. "Effect of SARA fractions on the physical, structural and dynamic properties of bitumen using molecular dynamics simulation." Construction and Building Materials 392: 132097.

Liu, Yongjian, Zhenlong Shen, Jiang Liu, Sha Chen, Jianping Wang, and Xiaolong Wang. 2022. "Advances in the application and research of steel bridge deck pavement." Structures.

Luo, Lei, Longjia Chu, and TF Fwa. 2021. "Molecular dynamics analysis of oxidative aging effects on thermodynamic and interfacial bonding properties of asphalt mixtures." Construction and Building Materials 269: 121299.

Luo, Sang, Jia Sun, Jing Hu, and Shicheng Liu. 2022. "Performance evolution mechanism of hot-mix epoxy asphalt binder and mixture based on component characteristics." Journal of Materials in Civil Engineering 34 (9): 04022235.

Mohammadi, Maryam, and Jamal Davoodi. 2017. "The glass transition temperature of PMMA: A molecular dynamics study and comparison of various determination methods." European Polymer Journal 91: 121-133.

Montazeri, Arash, Khalil Pourshamsian, and Mehran Riazian. 2012. "Viscoelastic properties and determination of free volume fraction of multi-walled carbon nanotube/epoxy composite using dynamic mechanical thermal analysis." Materials & Design (1980-2015) 36: 408-414.

Nie, Fenghua, Cheuk Lun Chow, and Denvid Lau. 2022. "A review on multiscale modeling of asphalt: development and applications." Multiscale Science and Engineering 4 (1): 10-27.

Nieuwenhuijsen, Mark J. 2016. "Urban and transport planning, environmental exposures and health-new concepts, methods and tools to improve health in cities." Environmental Health 15 (1): S38. https://doi.org/10.1186/s12940-016-0108-1.

Qiao, Yaning, Andrew R. Dawson, Tony Parry, Gerardo Flintsch, and Wenshun Wang. 2020. "Flexible Pavements and Climate Change: A Comprehensive Review and Implications." Sustainability 12 (3): 1057.

Shan, Bailin, Xuejuan Cao, Zengheng Hao, Yan Wu, Xiaoyu Yang, and Xiaoyan Li. 2024. "Experimental and Molecular Dynamics Simulations Investigating the Flexibility and Compatibility of Epoxidized Soybean Oil–Reinforced Epoxy Asphalt." Journal of Materials in Civil Engineering 36 (10): 04024327.

Sharma, Sumit, Rakesh Chandra, Pramod Kumar, and Navin Kumar. 2016. "Mechanical properties of carbon nanofiber reinforced polymer composites-molecular dynamics approach." Jom 68: 1717-1727.

Shokuhfar, Ali, and Behrouz Arab. 2013. "The effect of cross linking density on the mechanical properties and structure of the epoxy polymers: molecular dynamics simulation." Journal of molecular modeling 19: 3719-3731.

State Administration of Market Supervision and Administration. 2018. Plastics - Determination of tensile properties. GB/T 1040.1-2018. Beijing.

Sun, Jia, Wei Huang, Guoyang Lu, Sang Luo, and Youheng Li. 2023. "Investigation of the performance and micro-evolution mechanism of low-content thermosetting epoxy asphalt binder towards sustainable highway and bridge decks paving." Journal of Cleaner Production 384: 135588.

Sun, Jia, Sang Luo, Wei Huang, Jing Hu, and Shicheng Liu. 2023. "Structural optimization of steel bridge deck pavement based on mixture performance and mechanical simulation." Construction and Building Materials 367: 130217.

Sun, Jia, Sang Luo, Wei Huang, and Youheng Li. 2023. "Reducing epoxy resin content in a thermosetting epoxy asphalt mixture: A feasible method to facilitate application." Journal of Materials in Civil Engineering 35 (10): 04023352.

Sun, Jia, Zengping Zhang, Li Wang, Hao Liu, Xiaoyi Ban, and Junjie Ye. 2022. "Investigation on the epoxy/polyurethane modified asphalt binder cured with bio-based curing agent: Properties and optimization." Construction and Building Materials 320: 126221.

ul Haq, Muhammad Faizan, Naveed Ahmad, Muhammad Jamal, Waqas Anwar, Anwar Khitab, and Sabahat Hussan. 2020. "Carbon nanotubes and their use for asphalt binder modification: a review." Emerging Materials Research 9 (2): 234-247.

Wang, Zhijin, Yuanbin Zhou, Jiandong Zhang, Xinlv Ji, and Haifei Zhan. 2025. "Molecular components and molecular modelling for asphalt: A review." Advanced Physics Research 4 (4): 2400128.

Wiederhorn, Sheldon M., Richard J. Fields, Samuel Low, Gun-Woong Bahng, Alois Wehrstedt, Junhee Hahn, Yo

Tomota, Takashi Miyata, Haiqing Lin, Benny D. Freeman, Shuji Aihara, Yukito Hagihara, and Tetsuya Tagawa. 2011. "Mechanical Properties." In Springer Handbook of Metrology and Testing, edited by Horst Czichos, Tetsuya Saito and Leslie Smith, 339-452. Berlin, Heidelberg: Springer Berlin Heidelberg.

Williams, Malcolm L, Robert F Landel, and John D Ferry. 1955. "The temperature dependence of relaxation mechanisms in amorphous polymers and other glass-forming liquids." Journal of the American Chemical society 77 (14): 3701-3707.

Xu, Wen-Sheng, and Karl F. Freed. 2014. "Influence of Cohesive Energy and Chain Stiffness on Polymer Glass Formation." Macromolecules 47 (19): 6990-6997.

Yao, Hui, Junfu Liu, Mei Xu, Jie Ji, Qingli Dai, and Zhanping You. 2022. "Discussion on molecular dynamics (MD) simulations of the asphalt materials." Advances in Colloid and Interface Science 299: 102565.

Yu, Caihua, Kui Hu, Yujing Chen, Wengang Zhang, Yan Chen, and Rong Chang. 2021. "Compatibility and high temperature performance of recycled polyethylene modified asphalt using molecular simulations." Molecular Simulation 47 (13): 1037-1049.

Zhang, Fenglei, Pengfei Yao, Xiaoxuan Guo, Lei Zhang, and Kai Huang. 2023. "Study on the performance of epoxy asphalt with different matrix asphalt contents." Journal of Materials in Civil Engineering 35 (10): 04023339.

Zhang, Zengping, Jia Sun, Zhigang Huang, Feng Wang, Meng Jia, Wenjiang Lv, and Junjie Ye. 2021. "A laboratory study of epoxy/polyurethane modified asphalt binders and mixtures suitable for flexible bridge deck pavement." Construction and Building Materials 274: 122084.